



Nonlinear optical oscillation dynamics in high-Q lithium niobate microresonators

XUAN SUN,^{1,*} HANXIAO LIANG,^{2,*} RUI LUO,¹ WEI C. JIANG,¹
XI-CHENG ZHANG,¹ AND QIANG LIN^{1,2}

¹Institute of Optics, University of Rochester, Rochester, NY 14627, USA

²Department of Electrical and Computer Engineering, University of Rochester, Rochester, NY 14627, USA

*These authors contributed equally to this work

*qiang.lin@rochester.edu

Abstract: Recent advance of lithium niobate microphotonic devices enables the exploration of intriguing nonlinear optical effects. We show complex nonlinear oscillation dynamics in high-Q lithium niobate microresonators that results from unique competition between the thermo-optic nonlinearity and the photorefractive effect, distinctive to other device systems and mechanisms ever reported. The observed phenomena are well described by our theory. This exploration helps understand the nonlinear optical behavior of high-Q lithium niobate microphotonic devices which would be crucial for future application of on-chip nonlinear lithium niobate photonics.

© 2017 Optical Society of America

OCIS codes: (130.3990) Micro-optical devices; (130.3730) Lithium niobate; (190.4390) Nonlinear optics, integrated optics; (190.4870) Photothermal effects; (190.5330) Photorefractive optics.

References and links

1. K. J. Vahala, "Optical microcavities," *Nature* **424**, 839–846 (2003).
2. V. B. Braginsky, M. L. Gorodetsky, and V. S. Ilchenko, "Quality factor and nonlinear properties of optical whispering-gallery modes," *Phys. Lett. A* **137**, 393–397 (1989).
3. V. S. Ilchenko and M. L. Gorodetsky, "Thermal nonlinear effects in optical whispering gallery microresonators," *Laser Phys.* **2**, 1004–1009 (1992).
4. T. Carmon, L. Yang, and K. J. Vahala, "Dynamical thermal behavior and thermal selfstability of microcavities," *Opt. Express* **12**, 4742–4750 (2004).
5. A. E. Fomin, M. L. Gorodetsky, I. S. Grudinin, and V. S. Ilchenko, "Nonstationary nonlinear effects in optical microspheres," *J. Opt. Soc. Am. B* **22**, 459–465 (2005).
6. T. J. Johnson, M. Borselli, and O. Painter, "Self-induced optical modulation of the transmission through a high-Q silicon microdisk resonator," *Opt. Express* **14**, 817–831 (2005).
7. W.-S. Park and H. Wang, "Regenerative pulsation in silica microspheres," *Opt. Lett.* **32**, 3104–3106 (2007).
8. C. Schmidt, A. Chipouline, T. Pertsch, A. Tünnermann, O. Egorov, F. Lederer, and L. Deych, "Nonlinear thermal effects in optical microspheres at different wavelength sweeping speeds," *Opt. Express* **16**, 6285–6301 (2008).
9. L. He, Y.-F. Xiao, J. Zhu, S. K. Ozdemir, and L. Yang, "Oscillatory thermal dynamics in high-Q PDMS coated silica toroidal microresonators," *Opt. Express* **17**, 9571–9581 (2009).
10. M. W. Lee, C. Grillet, C. Monat, E. Mägi, S. Tomljenovic-Hanic, X. Gai, S. Madden, D.-Y. Choi, D. Bulla, B. Luther-Davies, and B. J. Eggleton, "Photosensitive and thermal nonlinear effects in chalcogenide photonic crystal cavities," *Opt. Express* **18**, 26695–26703 (2010).
11. M. Brunstein, A. M. Yacomotti, I. Sagnes, F. Raineri, L. Bigot, and A. Levenson, "Fast thermo-optical excitability in a two-dimensional photonic crystal," *Phys. Rev. A* **85**, 031803(R) (2012).
12. C. Baker, S. Stapfner, D. Parrain, S. Ducci, G. Leo, E. M. Weig, and Ivan Favero, "Optical instability and self-pulsing in silicon nitride whispering gallery resonators," *Opt. Express* **20**, 29076–29089 (2012).
13. Y. Deng, R. Flores-Flores, R. K. Jain, and M. Hossein-Zadeh, "Thermo-optomechanical oscillations in high-Q ZBLAN microspheres," *Opt. Lett.* **38**, 4413–4416 (2013).
14. D. M. Abrams, A. Slawik, and K. Srinivasan, "Nonlinear oscillations and bifurcations in silicon photonic microresonators," *Phys. Rev. Lett.* **112**, 123901 (2014).
15. J. Yang, T. Gu, J. Zheng, M. Yu, G.-Q. Lo, D.-L. Kwong, and C. W. Wong, "Radio frequency regenerative oscillations in monolithic high-Q/V heterostructured photonic crystal cavities," *Appl. Phys. Lett.* **104**, 061104 (2014).
16. W. Weng, J. D. Anstie, P. Abbott, B. Fan, T. M. Stace, and A. N. Luiten, "Stabilization of a dynamically unstable opto-thermo-mechanical oscillator," *Phys. Rev. A* **91**, 063801 (2015).
17. Q. Wang, Y. Wang, Z. Guo, J. Wu, and Y. Wu, "Thermal oscillatory behavior analysis and dynamic modulation of refractive index in microspherical resonator," *Opt. Lett.* **40**, 1607–1610 (2015).

18. S. Diallo, G. Lin, and Y. K. Chembo, "Giant thermo-optical relaxation oscillations in millimeter-size whispering gallery mode disk resonators," *Opt. Lett.* **40**, 3834–3837 (2015).
19. H. Itobe, Y. Nakagawa, Y. Mizumoto, H. Kangawa, Y. Kakinuma, and T. Tanabe, "Bi-material crystalline whispering gallery mode microcavity structure for thermo-opto-mechanical stabilization," *AIP Advance* **6**, 055116 (2016).
20. J. Wang, B. Zhu, Z. Hao, F. Bo, X. Wang, F. Gao, Y. Li, G. Zhang, J. Xu, "Thermo-optic effects in on-chip lithium niobate microdisk resonators," *Opt. Express* **24**, 21869–21879 (2016).
21. C. Wang, M. J. Burek, Z. Lin, H. A. Atikian, V. Venkataraman, I-C. Huang, P. Stark, and M. Lončar, "Integrated high quality factor lithium niobate microdisk resonators," *Opt. Express* **22**, 30924–30933 (2014).
22. J. Lin, Y. Xu, Z. Fang, M. Wang, J. Song, N. Wang, L. Qiao, W. Fang, and Y. Cheng, "Fabrication of high-Q lithium niobate microresonators using femtosecond laser micromachining," *Sci. Rep.* **5**, 8072 (2015).
23. J. Wang, F. Bo, S. Wan, W. Li, F. Gao, J. Li, G. Zhang, and J. Xu, "High-Q lithium niobate microdisk resonators on a chip for efficient electro-optic modulation," *Opt. Express* **23**, 23072–23078 (2015).
24. W. C. Jiang and Q. Lin, "Chip-scale cavity optomechanics in lithium niobate," *Sci. Rep.* **6**, 36920 (2016).
25. R. S. Weis and T. K. Gaylord, "Lithium niobate: Summary of physical properties and crystal structure," *Appl. Phys. A* **37**, 191–203 (1985).
26. L. Moretti, M. Lodice, F. G. D. Corte, and I. Rendina, "Temperature dependence of the thermo-optic coefficient of lithium niobate, from 300 to 515 K in the visible and infrared regions," *J. Appl. Phys.* **98**, 036101 (2005).
27. Y. S. Kim, and R. T. Smith, "Thermal expansion of lithium tantalate and lithium niobate single crystals," *J. Appl. Phys.* **40**, 4637–4641 (1969).
28. A. A. Savchenkov, A. B. Matsko, D. Strekalov, V. S. Ilchenko, and L. Maleki, "Enhancement of photorefraction in whispering gallery mode resonators," *Phys. Rev. B* **74**, 245119 (2006).
29. P. Günter and J.-P. Huignard, eds., *Photorefractive Materials and Their Applications 1, 2* (Springer, New York, 2006).
30. X. Sun, R. Luo, X.-C. Zhang, and Q. Lin, "Squeezing the fundamental temperature fluctuations of a high-Q microresonator," *Phys. Rev. A* **95**, 023822 (2017). Detailed discussion and formalization of thermo-optic nonlinear effect can be found in this paper.
31. P. Minzioni, I. Cristiani, V. Degiorgio, E. P. Kokanyan, "Strongly sublinear growth of the photorefractive effect for increasing pump intensities in doped lithium-niobate crystals," *J. Appl. Phys.* **101**, 116105 (2007).
32. H. Liang, W. C. Jiang, X. B. Sun, X.-C. Zhang, and Q. Lin, "Thermo-optic oscillation dynamics in a high-Q lithium niobate microresonator," *Proc. Conf. Lasers and Electro-Optics (CLEO)*, paper STu1E.4 (2016).

1. Introduction

High-quality (High-Q) optical microresonators, with the capability of significantly enhancing the optical field inside, offer ideal device platforms for studying nonlinear optical phenomena [1]. Among various nonlinear optical effects, the most common and well-known one is probably the thermo-optic nonlinearity [2–4]. The absorption by the device material converts a small fraction of optical power into heat which in turn shifts the cavity resonance via the thermo-refraction and/or thermal expansion, with an amount dependent on the optical energy inside the cavity.

Of particular interest is when a second mechanism arises inside a resonator to compete with the thermo-optic nonlinear effect, which would result in complex nonlinear instability of the optical wave inside the cavity. This situation has attracted considerable attention in the past decade to explore nonlinear optical dynamics in a variety of device and material systems [5–20], since understanding the underlying physics is crucial for the application of high-Q microresonators. To date, nonlinear optical oscillation and pulsation have been observed to result from the competition of thermo-refraction with optical Kerr effect [5, 7, 8], free carrier generation [6, 11, 14, 15], mechanical deformation [12, 13, 19, 20], thermal expansion [16, 18], thermo-refraction of the cladding layer [9], photosensitive effect [10], or a separate heat dissipation process [17].

Recently, there is significant development on the nanofabrication of lithium niobate (LN) photonic devices, which produces high-Q LN microresonators available on a chip-scale platform [21–24]. Lithium niobate exhibits unique material characteristics [25] with great potential for many applications. The availability of high-Q on-chip LN microresonators enables the exploration of enhanced nonlinear optical effects in the regime inaccessible to conventional means. In this paper, we show nonlinear oscillation and pulsation in high-Q LN microresonators, resulting from intriguing competition between the thermo-optic nonlinear effect and the photorefractive effect which is distinctive to other devices and mechanisms that have ever been reported [5–20]. We

present a theory to nicely describe the observed phenomena.

2. Experimental characterization

The device we employed is an x-cut LN microdisk resonator, with a thickness of 300 nm and a diameter of 90 μm , sitting on 2- μm -thick silica pedestal (Fig. 1(a), inset). The device exhibits an intrinsic optical Q of 8.3×10^5 for a quasi-TE polarized cavity mode located at 1511.10 nm with the electric field dominantly lying in the device plane (Fig. 1(b)). To explore the nonlinear optical behavior, we launched a continuous-wave (CW) laser into the cavity via an optical tapered fiber (Fig. 1(a)) and monitored the time-dependent waveform of the optical wave transmitted from the device. Figure 1(a) shows the schematic of the experimental setup. Coupling of the tapered fiber to the device results in a coupling depth of about 90% of the mode (Fig. 1(b), inset), corresponding to an optical Q of 5.3×10^5 for the loaded cavity.

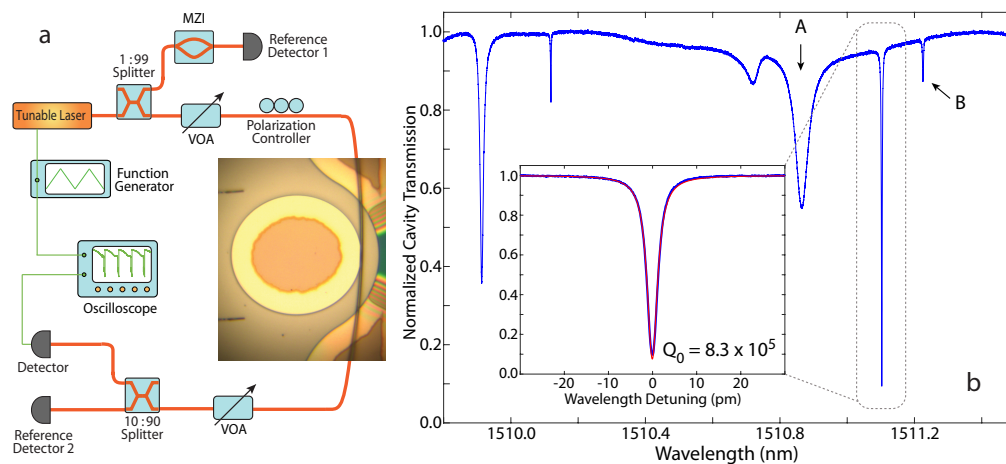


Fig. 1. (a) Schematic of the experimental setup, where the inset shows an optical microscopic image of the device coupled to a tapered optical fiber for light delivery into and out of the device. VOA: variable optical attenuator. MZI: Mach-Zehnder interferometer. (b) Laser scanned cavity transmission spectrum for the quasi-TE polarization. The inset shows the detailed transmission spectrum of the cavity mode at 1511.10 nm, with the experimental data in blue and the theoretical fitting in red. A and B denotes two cavity modes nearby.

We first scanned the laser wavelength across the cavity resonance back and forth in a periodic triangular fashion with a scanning rate of ~ 6 nm/s (Fig. 2(a), left panel), and recorded the transmission of the device. The left panel of Fig. 2 shows the detailed transmission waveforms at six different power levels. When the input optical power was low as $4.9 \mu\text{W}$, the device behaved linearly and the cavity transmission spectrum exhibited a normal Lorentzian shape (Fig. 2(b)). Interesting situation appeared when we increased the input optical power. When the laser wavelength was scanned from blue to red, the cavity transmission spectrum exhibited a typical bistability-type behavior. However, the overall position of the cavity resonance moved towards shorter wavelength with increased input power (Figs. 2(c)-2(g)), which is distinctive to conventional thermo-optic bistability [4]. On the other hand, when the laser wavelength was scanned from red to blue, the cavity transmission spectrum started to broaden and eventually showed significant oscillation. The onset of oscillation moved towards shorter wavelength with increased input power.

To further investigate the device behavior, we fixed the laser wavelength at a certain laser-cavity detuning and monitored the cavity transmission waveform. At a first glance, we would expect a normal thermo-optic locking [4] when we slowly tuned the laser wavelength towards the

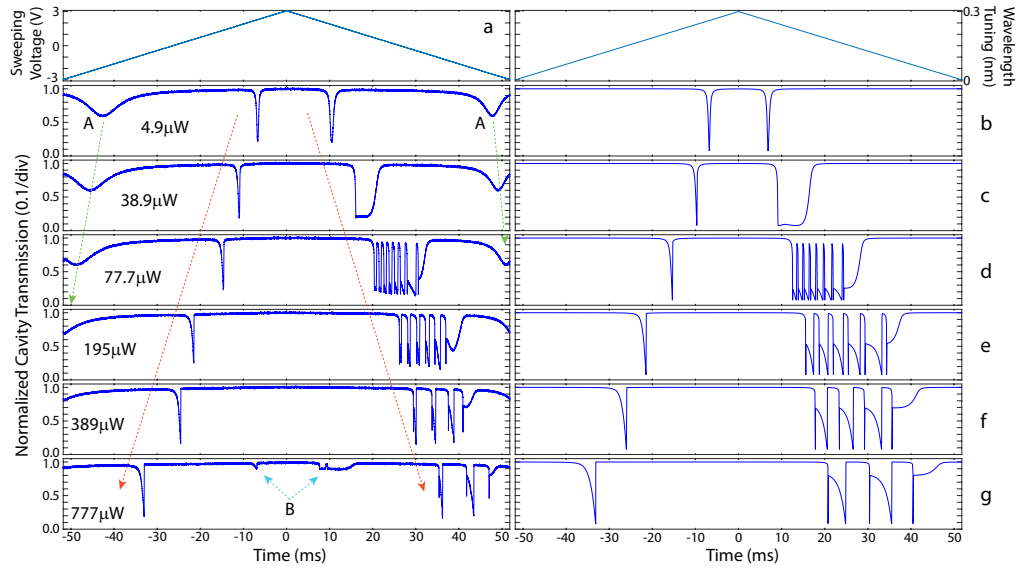


Fig. 2. Laser-scanned cavity transmission spectrum as a function of input optical power. Left panel: Experimentally recorded traces. (a) shows the sweeping voltage to piezoelectrically drive the laser cavity mirror. Accordingly, the laser wavelength is swept back and forth periodically with a scanning rate of ~ 6 nm/s. In (b)-(g), the red arrows indicate the overall blue shifting of the cavity resonance at 1511.10 nm. The green arrows indicate the corresponding blue shifting of a nearby mode, Mode A (see Fig. 1(b)). Light blue arrows indicate the nonlinear dynamics on Mode B (see Fig. 1(b)). Right panel: Theoretically modeled traces based on Eqs. (1)-(3). Detailed parameters are given in the text.

cavity mode at the blue detuned side, since the cavity transmission showed a typical thermo-optic bistability when the laser was scanned from blue to red (Fig. 2). Surprisingly, the cavity resonance jumped quickly and the laser-cavity detuning could not stay at a stable value, in strong contrast to the conventional thermo-optic locking phenomenon [4]. However, when the laser approached

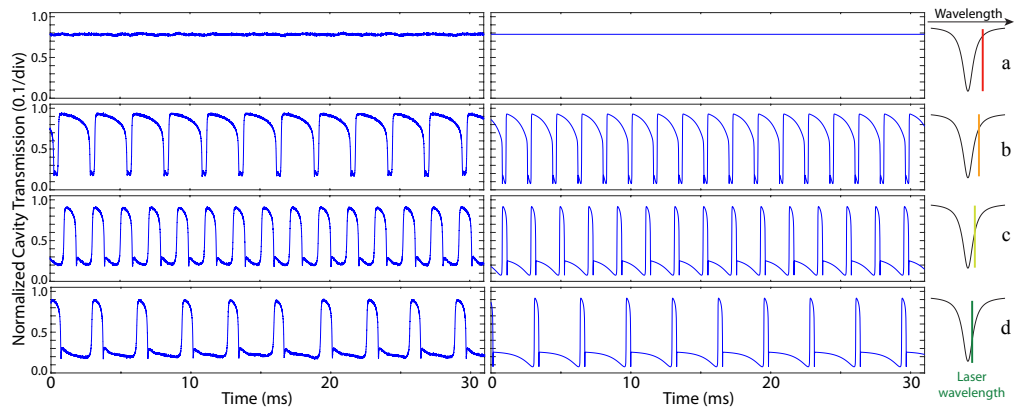


Fig. 3. Time-dependent waveform of cavity transmission at an input optical power of $77.7 \mu\text{W}$. The laser wavelength was set at four different wavelengths, as schematically illustrated on the right. Left panel: Experimentally recorded waveforms. Right Panel: Theoretical modeling based on Eqs. (1)-(3), with a fitted $\eta_E = 2.73 \text{ MV}/(\text{m} \cdot \text{fJ} \cdot \text{s})$.

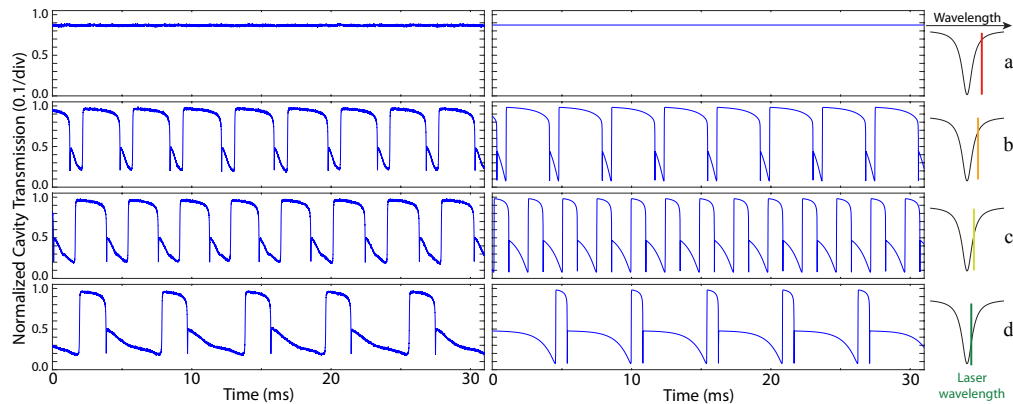


Fig. 4. Time-dependent waveform of cavity transmission at an input optical power of $155 \mu\text{W}$. The four laser wavelength settings are schematically illustrated on the right. Left panel: Experimentally recorded waveforms. Right Panel: Theoretical modeling based on Eqs. (1)-(3), with a fitted $\eta_E = 2.09 \text{ MV}/(\text{m} \cdot \text{fJ} \cdot \text{s})$.

the cavity resonance from the red detuned side, a stable laser-cavity detuning appeared when it stayed at a large value (Fig. 3(a), left panel). When we tuned the laser wavelength further into the cavity resonance, the cavity transmission started to oscillate, as shown in the left panel of Fig. 3(b), with a pulsing period of $\sim 2.6 \text{ ms}$. Further tuning the laser into the cavity mode caused the pulsing period to decrease first to $\sim 2.0 \text{ ms}$ (Fig. 3(c), left panel) and then increase again to $\sim 3.2 \text{ ms}$ (Fig. 3(d), left panel), while the duty cycle of the pulses decreases monotonically from Fig. 3(b) to Fig. 3(d). The exact pulsing waveform depends on the specific laser-cavity detuning (Figs. 3(b)-3(d), left panel). Further tuning the laser wavelength towards blue caused the cavity resonance to jump away quickly and the oscillation waveform disappears.

Similar phenomena were observed at higher power levels, as shown in Figs. 4 and 5. However, the pulsing periods increase to $\sim 3.9\text{--}5.8 \text{ ms}$ at input power of $155 \mu\text{W}$ (Fig. 4). Moreover, the pulse waveforms become flatter on the top compared with those in Fig. 3 and the falling

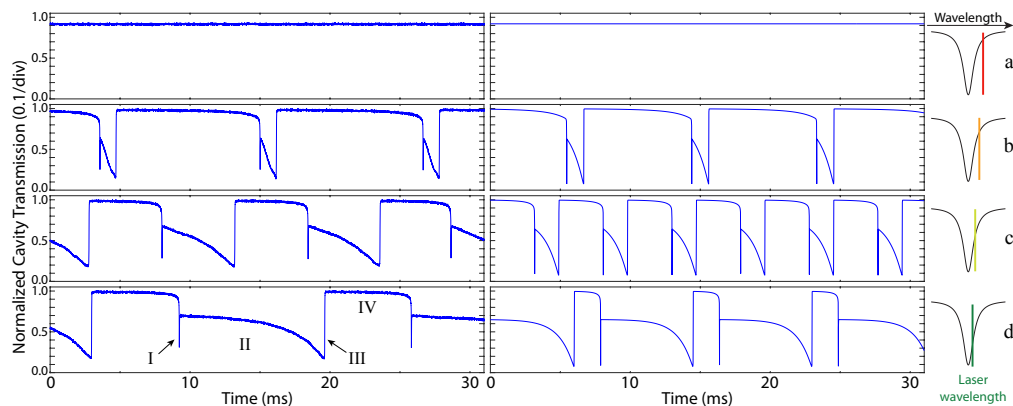


Fig. 5. Time-dependent waveform of cavity transmission at an input optical power of $309 \mu\text{W}$. The four laser wavelength settings are schematically illustrated on the right. Left panel: Experimentally recorded waveforms. In (d), the four numbers, I – IV, denote four time regions in which the cavity transmission shows different temporal dynamics. Right Panel: Theoretical modeling based on Eqs. (1)-(3), with a fitted $\eta_E = 1.62 \text{ MV}/(\text{m} \cdot \text{fJ} \cdot \text{s})$.

edges show a sharp dip. These phenomena become even more prominent when the input power increases. Figure 5 shows the case for an input power of $309 \mu\text{W}$, where the cavity transmission shows more square-like waveform with pulsing periods increasing significantly to $\sim 10\text{--}17 \text{ ms}$ whose exact value depends on the laser-cavity detuning.

We observed similar oscillation and pulsing dynamics on other cavity modes, regardless of their polarizations and mode species. One example is evident in a mode nearby, Mode B, indicated on Fig. 2, which also exhibits similar dynamic behaviors when the laser scans across the mode. The same phenomena were also observed on other devices regardless of the crystal orientation (x-cut or z-cut). These observations indicate the universal feature of the phenomena.

3. Physical interpretation

For a telecom-band wavelength, congruent single-crystalline lithium niobate at room temperature exhibits a positive thermo-optic coefficient of $\frac{dn_e}{dT} \approx 3.34 \times 10^{-5}/\text{K}$ for the extraordinary polarization and a negligible one for the ordinary light, $\frac{dn_o}{dT} \approx 0$ [26]. On the other hand, LN exhibits positive linear thermo-expansion coefficients of $\alpha_l^{(Z)} \approx 1.538 \times 10^{-5}/\text{K}$ and $\alpha_l^{(X,Y)} \approx 0.748 \times 10^{-5}/\text{K}$ along the crystal directions in parallel and perpendicular to the optical axis, respectively [27]. As a result, when the device is heated by optical absorption, both thermo-refraction and thermal expansion shift the cavity resonance towards a longer wavelength, functioning constructively to contribute to the thermo-optic nonlinearity.

The pulsing dynamics shown in Figs. 2-4 implies that certain nonlinear mechanisms compete inside the LN microresonator. Using Fig. 5(d) as an example, the pulsing waveform can be separated into four different temporal regions, where in Region I, the optical power dropping into the cavity triggers a fast cavity response to shift the cavity resonance, producing a sharp dip on the cavity transmission. As the initial laser wavelength is located at the red detuned side, this infers a fast *red shift* of the cavity resonance (see Fig. 6), which is likely to be dominantly induced by the thermo-optic nonlinear effect. Detailed analysis of the waveform shows that this fast response occurs in a time scale of $\sim 10 \mu\text{s}$, implying a temperature relaxation rate of $\sim 100 \text{ KHz}$ which is close to other devices of similar physical sizes [9]. The fast thermo-optic nonlinear response red shifts the cavity resonance across the laser wavelength, resulting in the laser located at the blue detuned side (Fig. 6).

In Region II, Fig. 5(d) shows that the cavity transmission decreases continuously till a minimum value. It infers that a second nonlinear mechanism starts to dominate and to counteract the thermo-optic nonlinearity, which shifts the cavity resonance towards *blue* (see Fig. 6). This process must relax at a speed much slower than the temperature relaxation and at a time scale

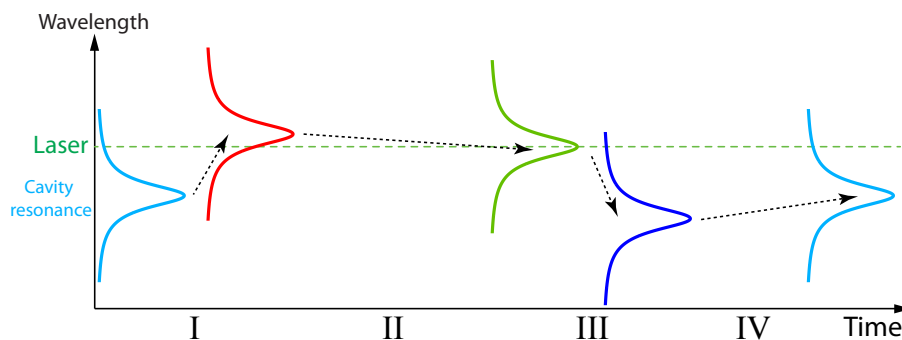


Fig. 6. Schematic of the time-dependent cavity resonance shift induced by the competition between the thermo-optic nonlinear process and the photorefractive process. Regions I–IV correspond to the four regions indicated in Fig. 5(d).

comparable to or even longer than the scanning period of the laser wavelength, so that it would eventually leave a net *blue shift* of the cavity resonance, since Fig. 2 shows an overall blue shift of the cavity resonance with a magnitude dependent on the optical power. As shown in Fig. 2, the blue resonance shift is also experienced by other cavity modes (say, Mode A in Figs. 1 and 2). These features are typical signatures of photorefraction in LN [28], implying that the photorefractive effect is likely to be responsible for the observed phenomena.

Figure 5(d) shows that, when the cavity transmission reaches a minimal value, it jumps abruptly back to unity in Region III. This is because the blue resonance shift eventually moves the center of the cavity resonance to coincide with laser wavelength (Fig. 6), resulting a minimum cavity transmission. As the photorefractive process is fairly slow, it would try blue shifting the resonance further. However, any further blue shift would decrease the intracavity energy which in turn decreases the magnitude of thermo-optic nonlinearity. As the device temperature relaxes much faster than the photorefractive effect, this process accelerates the blue shifting of the cavity resonance at a fast speed, resulting in an abrupt jump of cavity transmission in Region III (Figs. 6 and 5(d)). Consequently, the cavity resonance is far blue detuned from the laser wavelength, and only a tiny fraction of optical power can be input into the cavity which produces negligible nonlinear effect. As the photorefraction relaxes relatively slowly, the cavity resonance drifts at the same slow speed in Region IV (Fig. 6). Accordingly, the cavity transmission remains close to unity (5(d)), until a later time when the cavity mode drifts back close to the laser wavelength and a second pulsing period begins.

4. Theoretical analysis

The discussion in the previous section shows that the thermo-optic nonlinear effect and the photorefractive effect are the two dominant mechanisms responsible for the nonlinear dynamics observed in the LN microresonator. On one hand, the response of the thermo-optic nonlinearity is directly related to the dynamics of device temperature under photothermal heating [4, 5]. On the other hand, the photorefractive effect of LN is essentially the electro-optic effect from the space-charge electric field produced via photovoltaic drift current [29]. As a result, the cavity resonance frequency, ω_c , becomes dependent on the device temperature and the space-charge electric field as $\omega_c(\Delta\bar{T}, \bar{E}_{sp}) = \omega_0 + g_T \Delta\bar{T} + g_E \bar{E}_{sp}$, where $\Delta\bar{T}$ and \bar{E}_{sp} are the device temperature variation [5, 30] and the space-charge electric field, respectively, averaged over the optical mode field profile. $g_T \equiv \frac{d\omega_c}{dT}$ stands for the photothermal coupling coefficient and $g_E \equiv \frac{d\omega_c}{dE}$ represents the electro-optic coupling coefficient. ω_0 is the cavity resonance frequency of the passive cavity in the absence of thermo-optic nonlinear effect and photorefractive effect.

Therefore, the optical field inside the cavity can be described by the following equation [4,5,30]

$$\frac{da}{dt} = (i\Delta_0 - \Gamma_l/2)a - ig_T \Delta\bar{T}a - ig_E \bar{E}_{sp}a + i\sqrt{\Gamma_e}A, \quad (1)$$

where $\Delta_0 = \omega_l - \omega_0$ is the detuning of the laser frequency ω_l to the cavity resonance ω_0 . Γ_l and Γ_e are the photon decay rate and external coupling rate, respectively, of the loaded cavity. a and A are the amplitudes of the intracavity field and the input field, respectively, normalized such that $|a|^2$ and $|A|^2$ represent the intracavity energy and the input power, respectively.

The second term on the right hand side of Eq. (1) represents the thermo-optic effect, where the photothermal coupling coefficient is given by $g_T = -\omega_0(\alpha_n + \alpha_l)$ where α_n describes the effect of thermo-refraction and α_l describes the effect of thermal expansion. For simplicity, we have assumed that the thermo-refraction and thermal expansion respond to a same temperature variation $\Delta\bar{T}$. For a quasi-TE polarized cavity mode in an x-cut LN microdisk resonator, the optical field (dominantly polarized in plane) propagating inside the resonator becomes ordinary and extraordinary polarization equally probably. As a result, α_n is well approximated by $\alpha_n \approx \frac{1}{2} \left(\frac{1}{n_e} \frac{dn_e}{dT} + \frac{1}{n_o} \frac{dn_o}{dT} \right)$ where n_o and n_e are the refractive indices for the ordinary and extraordinary

polarizations, respectively. Similarly, α_l is well approximated by $\alpha_l \approx \frac{1}{2} [\alpha_l^{(Z)} + \alpha_l^{(X,Y)}]$. The mode-averaged temperature variation $\Delta\bar{T}$ satisfies the following equation [4, 5, 30]

$$\frac{d(\Delta\bar{T})}{dt} = -\Gamma_T \Delta\bar{T} + \eta_T |a|^2, \quad (2)$$

where Γ_T represents the thermal relaxation rate and η_T is the photothermal heating coefficient that is related to the optical absorption and heat conversion [5, 30].

The third term on the right hand side of Eq. (1) represents the electro-optic effect induced by the space-charge electric field. In LN, the space-charge electric field is dominantly produced via the photovoltaic drift current along the crystal axis [29]. As a result, for a quasi-TE polarized cavity mode in an x-cut LN microdisk resonator, detailed analysis shows that the electro-optic coupling coefficient $g_E \approx \frac{n^2}{4} \omega_0 (r_{13} + r_{33})$ where r_{13} and r_{33} are the electro-optic coefficients of LN. As the photovoltaic current is generally generated by asymmetric excitation of carriers via optical absorption [29], the dynamics of the space-charge electric field can thus be described by the following equation

$$\frac{d(\bar{E}_{sp})}{dt} = -\Gamma_E \bar{E}_{sp} + \eta_E |a|^2, \quad (3)$$

where Γ_E is the relaxation rate of the electric field and η_E is the field generation coefficient.

Equations (1)-(3) provide a complete set of equations to describe the cavity dynamics under the combined effect of thermo-optic nonlinearity and photorefractive. In Eqs. (1)-(3), g_T and g_E are known parameters related to the intrinsic properties of LN material [25–27]. Γ_e and Γ_l describes the linear properties of the LN microresonator, which can be obtained from the laser-scanned transmission spectrum of the cavity mode in the linear regime (Fig. 1(b)). The parameters related to the generation/relaxation of heat and space-charge field, Γ_T , η_T , Γ_E , and η_E , depend on both material properties and specific device geometry, which are generally unknown and difficult to obtain experimentally. To model the experimental results, we treat them as fitting parameters and numerically solve Eqs. (1)-(3).

Our detailed numeric modelings show that $\Gamma_T = 100$ kHz, $\eta_T = 375$ K/(fJ · s), $\Gamma_E = 15.7$ Hz, and $\eta_E = (1.2 - 3.7)$ MV/(m · fJ · s) provide the best description of the observed phenomena (It turns out that the field generation coefficient η_E is power dependent, which will be discussed in detail in the next section.). The right panels of Figs. 2-5 plot the simulated cavity transmission waveforms, in direct comparison with experimental results shown on the left. As shown in Fig. 2, the bistability-type behavior, the nonlinear oscillation, and the overall resonance blue shift are all quantitatively represented by the theory. Figure 3-5 show that the theory is able to reproduce the pulsing behaviors at all power levels and laser-cavity detunings. All these figures show clearly that the theoretical modeling based upon Eqs. (1)-(3) agree closely with the experimental observation.

To gain more insight into physics, we plot in Fig. 7 the detailed simulated waveforms of the cavity transmission, the induced temperature variation, the induced space-charge electric field, and the corresponding cavity resonance shifts, for an input power of 155 μ W at a laser-cavity detuning directly corresponding to Fig. 4(b). As shown clearly in Figs. 7(b) and 7(e), the photothermal heating process dominates in Region I to rapidly red shift the cavity resonance. Figures 7(c) and 7(d) show that it is the slow growth of the space-charge electric field that counteracts the thermo-optic effect in Region II, leading to a net blue shifting of the cavity resonance at a slow speed. Figures 7(b) and 7(e) show clearly that the rapid decrease of the device temperature in Region III accelerates the large blue shifting of the resonance, which causes an abrupt jump on the cavity transmission (Fig. 7(a)). As shown in Figs. 7(c) and 7(d), the slow relaxation of the space-charge electric field in Region IV introduces a slow drift of the cavity resonance towards the laser frequency. The slow accumulation of the intracavity optical

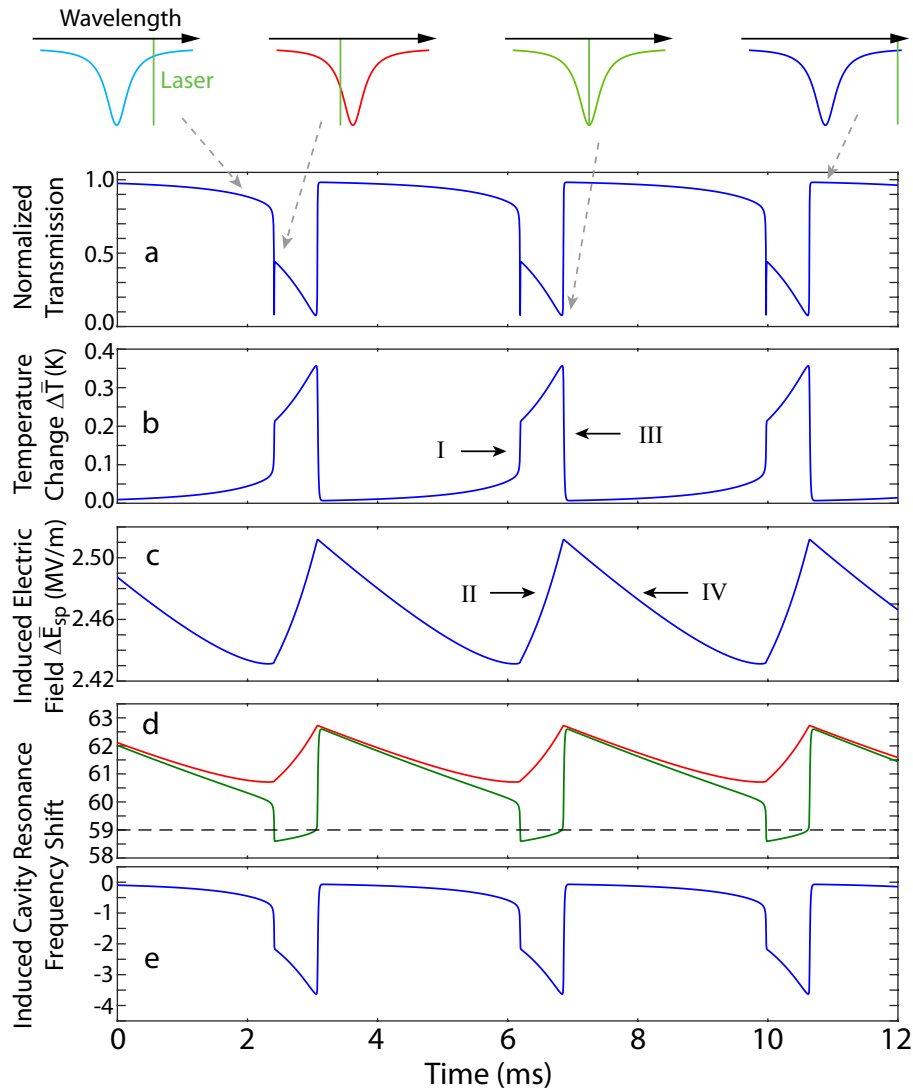


Fig. 7. Nonlinear optical dynamics of the device, numerically modeled by Eqs. (1)-(3). The input optical power is $155 \mu\text{W}$ same as Fig. 4. (a) Waveform of cavity transmission, directly corresponding to Fig. 4(b). (b) Temperature variation ΔT of the device induced by the photothermal heating. (c) Space-charge electric field \bar{E}_{sp} induced by the photorefractive effect. (d) and (e) The corresponding frequency shifts of the cavity resonance, induced by the thermo-optic effect (blue curve) and the photo-refractive effect (red curve), respectively. The green curve shows the net resonance frequency shift under the combination of these two effects. The plotted frequency shift is normalized by the linewidth, Γ_l , of the loaded cavity. A positive (negative) value infers a blue (red) shift of the resonance frequency (compared with the resonance frequency of the passive cavity in the absence of nonlinear effects). The dashed line indicates the laser frequency (with respect to the passive cavity resonance.) The four schematics on the top illustrate the laser-cavity detunings at the four typical points of the pulsing waveform. Note that the laser wavelength is fixed in the schematics, while the cavity resonance is shifted by different physical processes.

energy gradually heats up the device temperature (Fig. 7(b)), eventually leading to a second pulsing period. The dynamics of temperature variation and space-charge field shown in Fig. 7 clearly confirms the physical interpretation described in the previous section.

5. Discussions

On the relaxation of photorefraction

The theoretical modeling in the previous section shows that the photorefractive effect exhibits a relaxation rate of 15.7 Hz, corresponding to a relaxation time of 64 ms. To confirm such relaxation, we performed an independent ring-down measurement of the transmission spectrum of the cavity mode at 1511.10 nm. We first launched an optical power of 271 μW to the device and kept the periodic laser scanning of the mode for a certain time period until the cavity transmission spectrum is stable with the cavity resonance blue shifted (similar to the experiment in Fig. 2). We then switched the input power to a low value of 1.1 μW and monitored how the laser-scanned cavity transmission spectrum varies with time. As the nonlinear effects are negligible at this power level, the cavity resonance would relax naturally back to its original wavelength.

Figures 8(a) and 8(b) show the recorded time dependence of the cavity transmission spectra and the cavity resonance wavelength, respectively. They show clearly that the photorefractive effect does relax in a relatively slow pace. Interestingly, the relaxation of the cavity resonance wavelength does not exhibit a single exponential decay, as shown clearly in the inset of Fig. 8(b) which plots the same curve in the logarithmic scale. Such a complex relaxation behavior might be responsible for the slight discrepancy on the pulsing waveforms between theory and experiments shown in Figs. 2-5, as Eq. (3) assumes a single exponential relaxation.

By fitting the experimental data, we found that the relaxation of the cavity resonance exhibits three time constants, $\tau_1 = 50$ ms, $\tau_2 = 0.59$ s, and $\tau_3 = 2.38$ s. The first one is close to 64 ms obtained from the theoretical modeling in the previous section. These time scales of photorefraction relaxation in our device are quite small compared with that in bulk LN crystal [29] or in millimeter-size resonators [28]. The underlying physical nature is not known and requires further exploration. Note that our current ring-down measurement setup has limited time

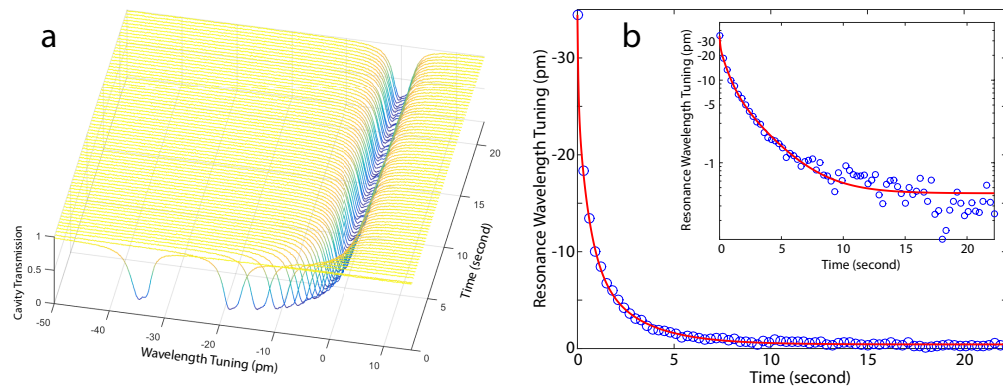


Fig. 8. Time-dependent relaxation of the cavity mode. (a) Laser-scanned transmission spectrum of the cavity mode as a function of time. (b) Time-dependent variation of the resonance wavelength, with experimental data shown as blue open circles and theoretical fitting shown as a red curve. The wavelength tuning is defined as the wavelength difference between the blue shifted wavelength and the intrinsic resonance wavelength of the passive cavity. The inset shows the same figure but in logarithmic scale for the vertical axis.

resolution and detailed characterization of the relaxation process below 0.1 s requires further investigation.

The multi-exponential relaxation of photorefraction observed in our devices is likely due to complex species of active centers existing in a LN crystal that trap free carriers [29]. As different types of active centers might have different rates of releasing the trapped carriers, the overall relaxation of space charge distribution would thus exhibit a complex relaxation behavior with multiple time constants. The exact physical nature will require further exploration.

On the generation of photorefraction

We compared the theoretical modeling with experiment characterizations at all power levels (some of which are shown in Fig. 2). Surprisingly, we found that the field generation coefficient η_E depends on optical power. The fitted values of η_E are plotted in Fig. 9, which shows clearly that η_E decreases with increased input optical power. It indicates that the generation efficiency of the space-charge electric field decreases with increased optical power, implying that the photorefractive effect in our device exhibits a certain sublinear behavior. Sublinear growth of the photorefractive effect was observed in the past, but only for doped LN crystals, not for undoped congruent LN [31]. The exact physical nature of the saturation behavior observed in our device is not known, which requires further exploration. Note that Fig. 9 only provides an indirect characterization of the saturation behavior, as it was obtained from theoretical modeling of complex dynamics based upon Eqs. (1)-(3). Future more direct measurement of the effect would help characterize the behavior in more detail and identify the underlying physics.

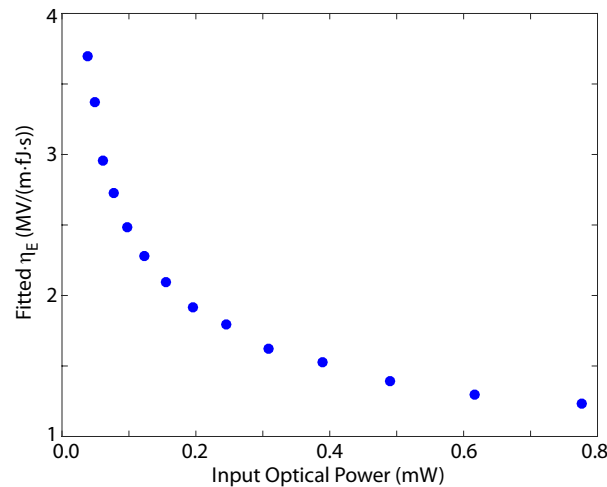


Fig. 9. Fitted η_E as a function of input optical power.

On the stable laser-cavity locking

Figures 3-5 focus on the red detuned regime of the cavity mode to show the nonlinear oscillation and pulsing. Previous discussions show that the cavity could become unstable when the laser is located at the blue detuned side. This situation, however, varies with device geometry. Depending on devices, a stable laser-cavity locking can be achieved on the blue-detuned side. It turns out that this regime cannot be accessed directly from the blue detuned side, where the cavity becomes unstable. However, we can access it by approaching the cavity resonance from the red detuned side instead, and then cross over the resonance into the stable laser-cavity locking regime. Figure 10 shows an example for a z-cut LN microdisk resonator [32]. It shows that, when the laser

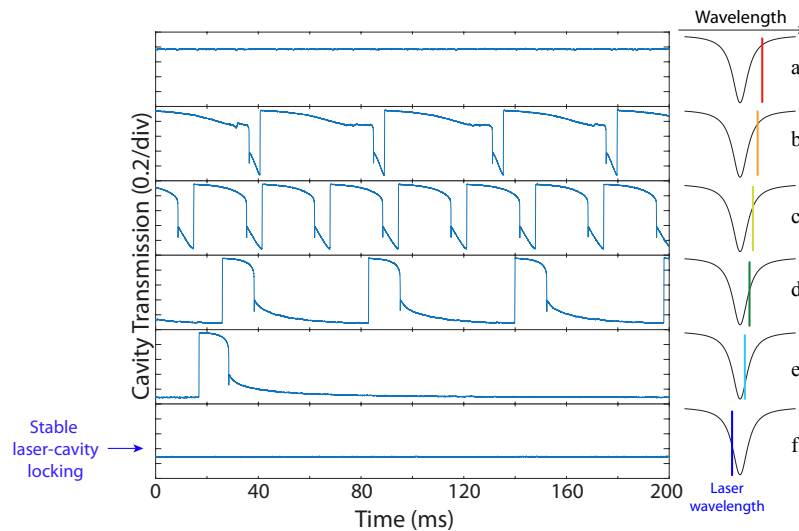


Fig. 10. Time-dependent waveforms of cavity transmission at various laser-cavity detunings, for a z-cut LN microdisk resonator with a diameter of $14 \mu\text{m}$, a thickness of 400 nm , and an intrinsic optical Q of 2.36×10^5 . The input optical power is $111 \mu\text{W}$.

approached the cavity resonance from the red detuned side, the device initially still experienced significant oscillation and pulsation. But further tuning the laser towards blue resulted in a stable laser-cavity locking, as shown clearly in Fig. 10(f). After falling into this regime, the stable locking can be maintained for a large range of laser-cavity detuning on the blue detuned side. The similar phenomena were observed in both z-cut and x-cut devices. The underlying physical mechanism for such procedure to achieve stable laser-cavity locking is potentially related to the saturation of photorefraction as well as its peculiar time response, which causes the thermo-optic nonlinearity to dominate when the laser wavelength falls into this regime. Accessing such a stable laser-cavity locking is crucial for many nonlinear optical applications.

6. Conclusion

In summary, we have shown experimentally complex nonlinear optical oscillation and pulsation dynamics in high-Q LN microresonators. The underlying mechanism stems from the intriguing competition between the thermo-optic nonlinear effect and the photorefractive effect that is unique to LN devices, distinctive to other mechanisms and device systems that have ever been reported [5–20]. We have developed a theory to reveal the essential underlying physics. Our exploration not only helps understand the nonlinear optical behavior of LN microphotonic devices that would be crucial for future application of on-chip nonlinear LN photonics, but also opens up a new window for future exploration of open questions related to complex behavior of photorefraction.

Funding

Defense Threat Reduction Agency; Defense Advanced Research Projects Agency SCOUT program (W31P4Q-15-1-0007); National Science Foundation (ECCS-1610674, ECCS-1509749); Army Research Office (W911NF-16-1-0436).

Acknowledgments

The authors thank Professor Gary Wicks at the University of Rochester for helpful discussions. This study was performed in part at the Cornell NanoScale Science and Technology Facility (CNF), a member of the National Nanotechnology Infrastructure Network.

This work was partially supported by the Defense Threat Reduction Agency, the Defense Advanced Research Projects Agency SCOUT program (W31P4Q-15-1-0007) from AMRDEC, and the National Science Foundation under grants No. ECCS-1610674 and ECCS-1509749.

This research was also sponsored by the Army Research Office and was accomplished under Grant Number W911NF-16-1-0436. The views and conclusions contained in this document are those of the authors and should not be interpreted as representing the official policies, either expressed or implied, of the Army Research Office or the U.S. Government. The U.S. Government is authorized to reproduce and distribute reprints for Government purposes notwithstanding any copyright notation herein.